Induced Voltage Estimation From Class EF Switching Harmonics in HF-IPT Systems

Nunzio Pucci , *Student Member, IEEE*, Juan M. Arteaga , *Member, IEEE*, Christopher H. Kwan, David C. Yates, *Member, IEEE*, and Paul D. Mitcheson , *Senior Member, IEEE*

Abstract—One of the advantages of high-frequency inductive power transfer systems is the high tolerance to misalignment and large air-gaps. However, the inherently large magnetic field volumes can lead to coupling of additional foreign objects with the primary, causing possible detuning of the system and heating of the objects. These foreign objects and the conditions of the local environment can load the transmitter, which changes the induced voltage on the primary side. Unfortunately, the induced voltage is not directly measurable in an operating transmitter and the most straightforward way of calculating this variable, through a measurement of primary coil current and voltage, can cause a significant decrease in quality factor which reduces system performance. An integrated solution capable of estimating the induced voltage through other less invasive measurements in the primary is needed to ensure safety of operation through foreign object detection. Knowledge of the induced voltage can also be used to correct tuning mismatches where both sides of the link are active (i.e., in synchronous rectification and bidirectional systems). In this article, multiple candidate variables for estimating the induced voltage are assessed based on factors such as measurement practicality and estimation accuracy. It is demonstrated for the first time that a solution which is based on the measurement of only two variables, the amplitude of the fundamental frequency of the switching waveform and input current, can achieve state-of-the-art induced voltage estimation accuracy. These two variables, which can be obtained using simple cost-effective analogue circuitry, are used in a Gaussian process to generate a regression model. This is used to estimate induced voltages at any angle in an approximate magnitude range of 0–20 V with a normalized root-mean-square error of 1% for the real part and 1.5% for the imaginary part. This corresponds to detecting a plastic container with 1 kg of saline solution (0.4% concentration, to emulate the electromagnetic profile of muscle) at a distance of 15 cm (1.5 coil radii). The results presented in this article were obtained with a bidirectional Class EF transceiver operating at 13.56 MHz delivering up to 32 W with coupling factors ranging from 1.1% to 4%. This article is accompanied by a video file demonstrating the experiments.

Index Terms—Class EF, foreign object detection (FOD), high frequency, induced voltage estimation, primary-side measurement, resonant power converter, wireless power transfer.

I. INTRODUCTION

THE development of high-efficiency inductive power transfer (HF-IPT) systems [1]–[4] has enabled wireless charging for new classes of applications in dynamic environments [5]–[8] because of the flexibility of systems operating in the megahertz range both from the perspective of low coupling operation [9], [10] and load variations [11]–[16].

While IPT systems which operate at tens and hundreds of kilohertz exploit flux shaping through the presence of ferrite, aiming to mitigate the effect of misalignment on system performance [17]–[20], HF-IPT systems most commonly employ air-core coils, thus generating an unconstrained flux which is dependent on the coil geometry. This achieves larger tolerance to misalignment, eliminating the need of ferromagnetic materials, but it also causes larger energized volumes around the primary, increasing the likelihood of foreign objects coupling with the system.

The presence of foreign objects can lead to undesirable operating conditions, which affect system performance: When a foreign object reflects a reactance to the primary side, the resonant tank gets detuned, and this tends to cause additional losses (heating) in the system. Foreign objects can also heat up, making the environment where the system is operated unsafe for users.

Knowledge of the elements that are coupled to the primary coil is not only advantageous from a safety perspective. Estimating the induced voltage in the primary also allows tuning mismatches between primary and secondary in back-to-back active systems to be detected. Induced voltage estimation can also be used to minimize the reactive element of the reflected impedance by adjusting the relative phase between primary and secondary coil currents when using active receivers.

This article builds on the conceptual findings in our previous work [21], where we demonstrated that the drain voltage waveform of a Class EF inverter contains the information necessary to deduct the amplitude and phase of the induced voltage of a HF-IPT coil driven by the Class EF inverter, which we here generalize as a transceiver. However, the attainment of the estimated
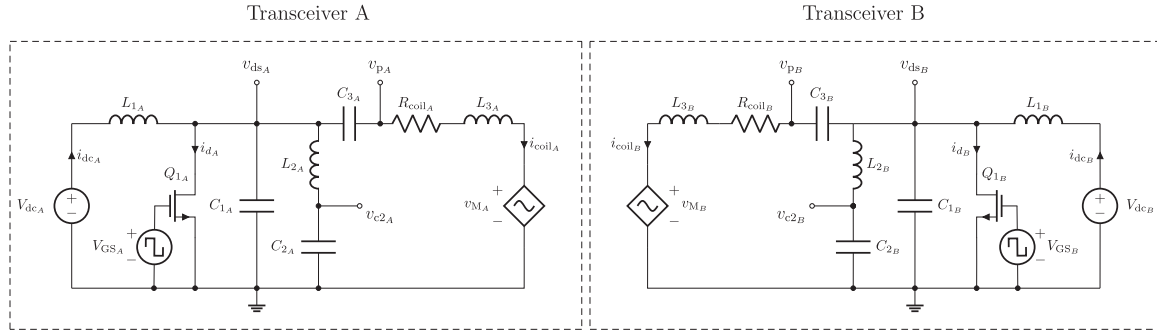
Fig. 1.   Circuit diagram of two bidirectional Class EF transceivers with the loads modeled as dependent voltage sources.

amplitude and phase of the induced voltage ($v_{\mathbf{M}}$[1]) requires high-performance oscilloscopes as a fundamental building block of the method. In this article, we focus on techniques that can be realized with simple and cost-effective hardware which are therefore suitable for integration into wireless power transfer systems for commercial deployment.

Specifically, we propose a technique to perform induced voltage estimations in real time based on the measurements of only two variables (selected following a statistical approach as detailed in Section V) in contrast with the work presented in [21], where the entirety of the time points of a sampled waveform is used. These two variables (input current and amplitude of the first harmonic of v_{c2} from the diagram in Fig. 1) only change when the link properties are modified (i.e., changes in load, coupling or the presence of a foreign object). This technique also makes it possible to overcome issues associated with high-frequency noise and sampling jitter, which are inherent of techniques that perform fitting of the entire time domain signal [21]. The proposed technique does not require high-performance instrumentation, as the entirety of the circuitry for extraction of the relevant signals can be implemented in a system submodule, with the possibility of miniaturization and integration in the system without compromising the tuning and the system efficiency.

The main contributions of this article are summarized as follows.

1) The work of [21] is susceptible to jitter in the measurement and it requires high-performance oscilloscopes to be implemented. In this work, the i_{dc_A}-H_1 variables are extracted as dc signals, eliminating the need of high-cost/high-bandwidth instrumentation. Additionally, this makes the effect of jitter in the measurement negligible.

2) The choice of a frequency domain method allows for a simplified and condensed alternative to extract the required information.

3) A method for variables selection based on correlation is presented, providing the designer with a tool to systematically assess what variables to use for model prediction in a given system.

4) The work presented in this article is extended for bidirectional operation of the transceiver, while in [21], the employed coil driver was just transmitting power.

[1]Phasors are presented in bold.

5) In Section V, an experimentally derived relationship, whose linear fit has an R^2 higher than 94%, is presented. This grants the possibility of integrating the system on a low-performance microprocessor if required, as the described model's complexity is low. With the model in [21], this would not be possible, as the model uses a large number of input variables, whose relationship with the output is not granted to be linear.

The rest of this article is organized as follows. Section II summarizes the key existing literature on foreign object detection (FOD) and Class EF coil drivers. Section III describes the practical variables to measure in a Class EF transceiver with the purpose of integrating an induced voltage estimation module in the complete system. Section IV describes the experimental setup and the data-gathering process used in this work. Section V explains the criteria to choose the optimal variables for model generation following a statistical approach. Section VI shows how the models for induced voltage estimation are generated, providing an overview of their performance. Section VII shows examples of practical applications of this article. Finally, Section VIII concludes this article.

II. BACKGROUND

A. Foreign Object Detection Prior Art

As covered in the review article [22], FOD in IPT systems is tackled by either employing external sensors (typically temperature or pressure), performing electrical system parameter readings, using wave-based detection (i.e., cameras and ultrasonic sensors), or field-based detection methods.

Field-based and wave-based detection techniques can achieve medium and high precision respectively. As explained in [22], this scales with the cost. Achieving a high degree of precision using techniques that are based on system parameter reading can prove challenging, but the required cost of such techniques is relatively low.

Electrical system parameter readings such as measurement of coil inductance and quality factor can prove challenging in HF-IPT systems, since the quality factor of the coils is typically higher than 500, making it difficult to perform a reliable measurement. While methods that are based on power loss, efficiency, or input current reading are feasible and provide cost-effective solutions for the purpose of FOD, the work in

this article provides an alternative low-cost method (less than 30 USD as shown in Table IV), in which the load does not have to be fixed and only primary-side readings are required. Estimations of the induced voltage also enable further applications such as synchronous rectification and load profiling as shown in Section VII.

B. FOD Through Induced Voltage Estimation

The effect of external objects on the primary can be modeled as a voltage source representing the induced voltage in series with the transmitter coil. Knowledge of the real and imaginary components of the induced voltage from other circuits or objects can allow detection of deviations from typical operation. This also enables the possibility of detecting tuning mismatches between primary side and secondary side, which can be used in multicoil systems [23] and active systems to adjust the power flow by changing the relative phases of the coils currents of the transceivers. For the aforementioned reasons, it is advantageous to gather information on the induced voltage through a solution which is integrated in the IPT system.

Measuring the induced voltage in a HF-IPT system comes with several practical challenges. In mid-power applications, the voltage across the primary coil can approach the kilovolts range, making it difficult to be probed directly. Any instrumentation added across the primary coil would lead to detuning, since at these frequencies, even several picofarads can alter the resonant point of the link.

It is possible to estimate the induced voltage on the primary while knowing the magnitude and phase of the current in the primary and secondary coils, their self-inductances, and mutual coupling; however, this would require simultaneously probing both sides and using high-performance active current probes for the measurement. This knowledge can however be used to infer a relationship between other measurable variables of the system and the induced voltage on the primary side.

In [21] and [24]–[26], we have proposed new electrical-parameter-based techniques for FOD in HF-IPT systems: A variation in the induced voltage on the primary is inferred based on the shape of the switching waveforms of the transceiver. These techniques show promising results [the normalized root-mean-square error (RMSE) is lower than 2%], but they are difficult to implement in a deployed system since the waveforms are recorded using high-performance oscilloscopes.

This issue can be overcome using the methods based on subsampling or interpretation of the harmonic content of the switching waveform proposed in the following sections of this article, allowing for cost-effective deployment of this technique for HF-IPT systems.

C. Implementing Class EF Transceivers for Bidirectional Wireless Power Transfer

Class EF [27] (see Fig. 1) is a coil driver topology that is typically employed in HF-IPT systems due to its high efficiency at MHz frequencies [1], [4]. This topology comes with the advantages of using only one low-side transistor and open-loop operation (constant duty cycle and frequency). As shown in [27]

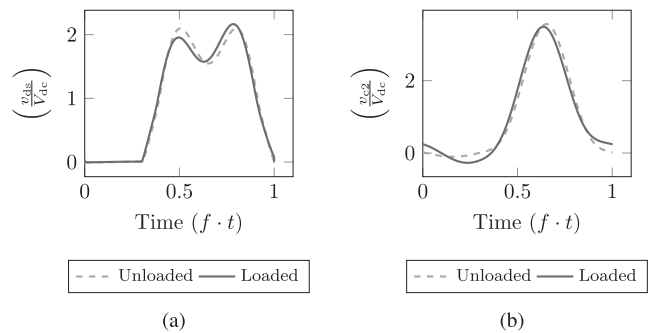| Component	Value	Description
C_1 (pF)	$100+C_{oss}$	Vishay QUAD HIFREQ
C_2 (pF)	186	Vishay QUAD HIFREQ
C_3 (pF)	125	Vishay QUAD HIFREQ
L_1 (μH)	88	Wurth Elektronik WE-PD
L_2 (nH)	234	Coilcraft 2014VS
L_p & L_s (nH)	1181	IPT PCB coils
Q_1		GS66504B (650 V, 15 A) GaN FET

Fig. 2. Theoretical waveforms of a load-independent Class EF inverter loaded and unloaded; the loads (as induced voltages) are 0 and 20 V with an angle of 0°. (a) v_{ds}. (b) v_{c2}.

and [28], this topology can be employed as an inverter or a rectifier: Power flow is controlled through the relative phase of the switching signals of the coil drivers, aiming for an angle between coil currents of $\pm90°$ to prevent imaginary reflected impedances [29]. The topology is similar to a Class E inverter, but the addition of L_2 and C_2 grants the possibility of waveform shaping, with the option of load-independent operation [11], [28] and an overall lower v_{ds} peak voltage.

The Class EF inverter presented in this article operates at a fixed frequency of 13.56 MHz and a fixed duty cycle of 30%. The choice of components can be found in Table I. The theoretical waveforms of this design are shown in Fig. 2. From these waveforms, it is noticeable that v_{ds} is zero at turn-ON for $|\boldsymbol{v_M}|$ values of 0 and 20 V. v_{c2} is a filtered version of v_{ds}, obtained across the capacitor of the EF branch.

As demonstrated experimentally in our previous work [21], a change in $\boldsymbol{v_M}$ yields a unique change in v_{ds}, and hence also in v_{c2}.

D. Effects of Nonlinearity in Gallium Nitride Field Effect Transistors (GaN FETs) on Analytical Modeling of HF-IPT Systems

While it is possible to analyze the presented circuit topology using state-space or first order approximation, the nonlinearity with respect to drain-source voltage introduced by the device's drain current [30] and parasitic capacitances (mostly the output capacitance C_{oss} [31], [32]), makes it challenging to obtain an analytical expression for the induced voltage as a function of other system parameters. In the specific case of series-tuned IPT systems operating in the megahertz range, in which the

chosen parallel capacitance is in the order of hundreds-of-pico-farads, C_{oss} becomes nonnegligible [33] when compared with the system's passive components. The presence of such parasitics increases the complexity of the state space, which can only be described through high-order differential equations, hence requiring numerical methods to be solved.

The technique presented in this article is based on coil driver characterization and fit of an appropriate function to map the induced voltage to a set of electrical parameters on the primary side, hence minimizing the effect of possible errors generated when describing the system through approximations in the modeling stage.

III. EVALUATION AND ATTAINMENT OF ELECTRICAL SIGNALS IN A CLASS EF TRANSCEIVER

In this article, the loading state of a transceiver is defined as the set of electrical parameters that define the behavior of the system under different loading conditions. This includes load, direction of power flow, losses, and changes in resonant point of the tank. It is possible to assess the loading state of a Class EF transceiver by analyzing the currents and voltages of the circuit diagram in Fig. 1.

While most of the parameters marked in the diagram in Fig. 1 are relevant to assess the loading state of the transceiver, not all of them are practical from an electrical measurement standpoint. The main variables are discussed as follows.

1) Primary Coil Current (i_{coil}) and Primary Coil Voltage (v_p): Resonant tank parameters such as Q factor and reflected impedance can be calculated knowing the primary coil current and voltage. Despite the measurement of these variables being popular and effective for parameter identification in kilohertz IPT systems [34], there are several challenges associated with systems operating in the megahertz range. Coil current measurements can be unpractical in HF-IPT systems, as the introduction of instrumentation can lower the quality factor of the coil: For example, in the coils presented in this article, an additional series resistance of 100 mΩ would result in a decrease in quality factor of more than 30%. Measuring the voltage across the coil can be challenging as well, since it is not uncommon to observe voltages in the kilovolts range. Probing also introduces an additional capacitance in the resonant tank which can alter the resonant frequency of the tank or change the operating nature of the inverter.

2) Transistor Drain Current (i_d): While it is possible to extract valuable information on the loading state of the inverter from this variable, measuring the drain current introduces an additional series inductance at the drain terminal of the device, which is nonnegligible in the typical packaging of wide-bandgap devices, such as GaN.

3) Input Current (i_{dc}): The information contained in the input current can be useful, as its average strongly correlates with the real power delivered by the transceiver. Measurements of this variable can be performed with relative simplicity from the system integration standpoint. This can be done either with a current sense resistor or Hall-sensors and fluxgate as reported in the literature [35].

4) Transistor Drain Voltage (v_{ds}) and EF Branch Capacitor Voltage (v_{c2}): v_{ds} contains relevant information for estimation of the loading state of the transceiver. From v_{ds}, it is possible to deduct when the transceiver is operating under suboptimal conditions (transistor hard-switching or body diode conduction). All this information ties directly with the magnitude and angle of v_M, making v_{ds} a good candidate variable for induced voltage estimation as previously in [21]. v_{c2} is a filtered version of v_{ds} obtained across the capacitor in the EF branch. Its maximum $|dv/dt|$ is lower than the one of v_{ds}, implying less abrupt changes, but similarly to v_{ds}, its behavior can also provide relevant information for the estimation of v_M.

The introduction of either a voltage probe or instrumentation has little effect on the inverter's tuning: Typical ranges of the C_1 and C_2 capacitances in 13.56 MHz designs are in the hundreds-of-picofarads, while the parasitics introduced by the probes or the instruments are lower than 7.5 pF [36]. This does not cause a deviation of equivalent capacitance at those nodes by more than 10%.

While both waveforms are measurable with a voltage probe without any major adjustments, using instrumentation requires scaling of the waveform. This can be achieved by using a potential divider or alternatively separating the C_1 or C_2 capacitance into two, achieving an appropriately sized capacitive voltage divider.

Implementing a capacitive voltage divider is more convenient for the measurement of v_{c2}: The additional inductance from splitting the C_2 capacitance can be compensated in L_2. However, implementing a capacitive divider to measure v_{ds} is inconvenient: With regards to PCB design, it is necessary to minimize the distance between C_1 and the transistor to avoid the introduction of parasitic inductance, making the splitting of C_1 problematic. The same problem applies for the placement of a sense resistor to use the current through C_1 as a source of information. Current sensing in the $L_2 - C_2$ branch is not convenient either, as introducing a current sense resistor would lower the equivalent quality factor of L_2, hindering performance.

It can be concluded that v_{c2} is an overall better candidate to measure via custom instrumentation. In this article, v_{ds} is also analyzed to compare the obtained results with the work previously presented in [21].

A. Time-Domain Methods

Having established that the focus lies on the waveforms v_{ds} and v_{c2} due to their information content and measurement practicality, it is necessary to establish how to extract and interpret the information contained to estimate the induced voltage.

Our previous work [21] already demonstrated that the information in v_{ds} can be used to estimate v_M; however, all the measurements were performed using 2.5 giga-samples-per-second (GSa/s) oscilloscopes (HDO6104 A and HDO4034 A from Teledyne LeCroy). From simulation, the minimum required number of samples to capture phenomena such as hard switching and diode conduction in a 13.56-MHz system is around 150 per cycle, corresponding to 2 GSa/s. In order to make the approach in [21] more suitable for embedding into real applications, here we
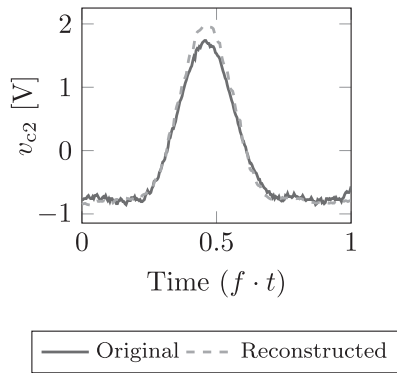
Fig. 3. Comparison of the original v_{c2} waveform obtained from an oscilloscope and the reconstructed v_{c2} waveform obtained with the subsampling method.

Fig. 4. Amplitude of harmonics 1–7 of v_{ds} and v_{c2} normalized to the sum of harmonics amplitude.

Fig. 5. Crystal characterization setup.

first propose a measurement technique based on subsampling. This can be implemented using a low-cost microprocessor (in this work, a Raspberry PI) controlling a delay module that triggers an ADC.

The process for extracting a periodic time domain waveform (v_{hf}) through subsampling consists of performing measurements at a frequency of $f_{samp} = f_{sw}/n$, where f_{sw} is the switching frequency and n is an arbitrary integer. This generates a measurement for a specific point in time within a cycle. By applying a controlled time-delay (t_d) to the trigger waveform generated at f_{samp}, it is possible to move to another point within v_{hf}. For a sufficiently small time-step, it is possible to obtain a reconstructed version of v_{hf}. The time resolution of the reconstructed waveform is given by the chosen value of t_d.

Fig. 3 shows a comparison between the original v_{c2} waveform extracted from an oscilloscope and its reconstructed version from the subsampled Raspberry Pi-based measurement. The RMSE normalized to the peak-to-peak of the original v_{c2} is around 1%, indicating a successful retrieval of the waveform through on-board instrumentation. The mismatch in the peak of v_{c2} is due to the additional parasitic inductance from the connection of the v_{c2} node to the subsampling circuit through a BNC-to-SMA cable and the difference in input impedances of the oscilloscope and the subsampling circuit.

B. Frequency Domain Methods

Changes in the induced voltage do not typically occur abruptly as they are caused by a change in load (where the rate of change is limited by the size of the output energy storage system) or a change in position of a foreign object or transceiver with respect to the primary. This means that the loading state of the transceiver remains practically unchanged in a time window during which its switching waveforms can be approximated with a Fourier series.

In most Class EF inverter designs, the majority of the power ($>90\%$ as shown in Fig. 4) is carried by the first, second, and third harmonics of the waveforms, and hence in this article, the frequency domain analysis is based on these frequencies only. As is shown in Section VI, the information contained in only
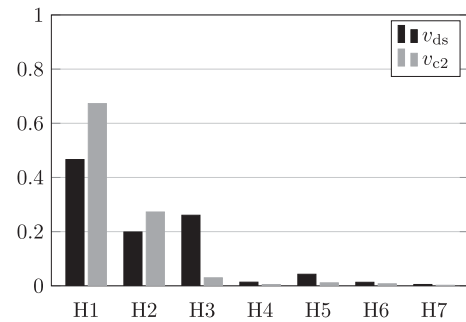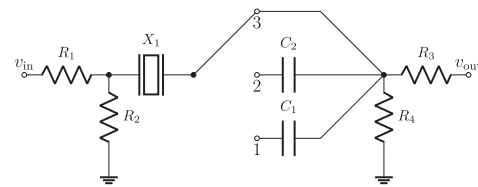
the first and second harmonics is sufficient to perform low error estimations of the induced voltage.

For the extraction of information in the frequency domain, it is necessary to perform three key steps: Harmonics separation, amplitude measurement of the individual sine-waves, and retrieval of phase difference. In our implementation, the harmonics are separated with bandpass filters. This requires the filter response to be close to unity gain in a very narrow band at the frequency of the desired harmonic, while achieving high attenuation for the other frequency components of the waveform. Obtaining this performance through classic active and passive filter topologies often requires high-order filters which have extreme sensitivity to passive components values. The availability of affordable operational amplifiers suitable for filtering in the megahertz range is another constraint. However, using a second-order quartz-crystal bandpass ladder filter can achieve a flat response for narrow passbands, making it a suitable filter type for this application [37].

The bandpass ladder filter is tuned after performing a characterization of the crystals. Using three different RC combinations at the output of the filter (as shown in Fig. 5) and measuring the frequency of resonance, it is possible to estimate the series inductance, series capacitance and parallel capacitance of the crystal. Following the design methodology illustrated in Chapter 3 of [38], the filter is tuned by neglecting the parallel capacitance (C_p) and achieving resonance of the motional inductance (L_m) and the combination of coupling capacitance (C_{12}) and motional capacitance (C_m). Both bandpass filters have a very narrow bandwidth as expected (1–10 kHz), with gains of $\simeq 1$ for the fundamental (13.56 MHz) and $\simeq 0.4$ for the second harmonic (27.12 MHz).

As shown in Fig. 6, the filtered waveform is then amplified (if necessary) to give a high enough voltage for the envelope detector to provide a $v_H > 0$ under all operating conditions. To
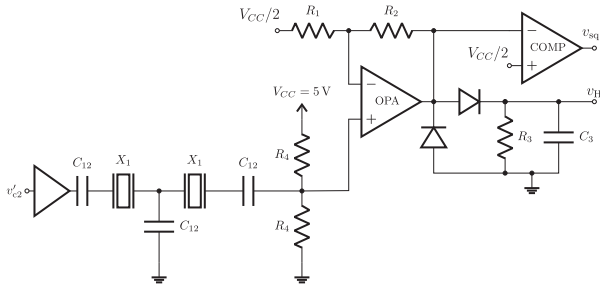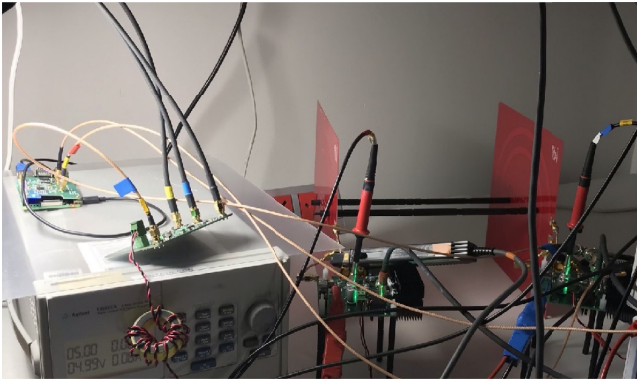
Fig. 6. Simplified diagram of a single side of the harmonics extraction circuit (v'_{c2} is a scaled version of v_{c2}).

(a)

(b)

Fig. 7. Experimental setup. (a) Test setup and equipment. (b) IPT link, 13.56 MHz coil drivers, and extraction boards on the left.

extract the 13.56 MHz component, the amplification is set to unity gain, while to extract the 27.12 MHz component, it is set to a gain of around 3. The phase difference is extracted using a type II phase detector, whose output is low-pass-filtered to obtain a dc signal.

IV. EXPERIMENTAL SETUP FOR GATHERING DATA ON THE LOADING STATE OF THE TRANSCEIVER

To generate a model that enables predictions of v_M for real applications, we first need to gather a set of data from the primary transceiver. This is done using the bidirectional test rig presented
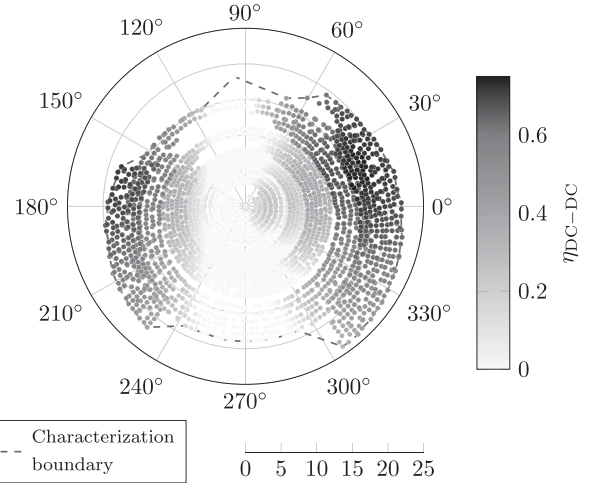

Fig. 8. Phasor chart representing the obtained dc–dc efficiency for different v_M values.

in [39] (see Fig. 7), together with the additional circuits for waveform extraction presented in Sections III-A and B.

The data are gathered using two identical Class EF transceivers (see Fig. 1). The transceiver to characterize, Transceiver A, is kept at a fixed input voltage, while Transceiver B is used to produce a measurable induced voltage onto Transceiver A. The phase (θ) between V_{GS_A} and V_{GS_B} changes the angle of the induced voltage, while the input voltage of Transceiver B (V_{dc_B}) and the coupling between the two coils (k) influence the magnitude of the induced voltage. The phase between the transmitter and receiver side is bounded by the operating region shown in Fig. 8. The phase value is changed in fixed steps of 2.5°. Five different couplings are used: 1.1%, 1.6%, 2.2%, 3.2%, and 4%. For the 1.1% coupling case, V_{dc} is stepped from 0 to 80 V in steps of 10 V. For couplings between 1.6% and 4%, V_{dc} goes from 60 to 80 V in variable steps to obtain an approximate distance between v_M samples of 0.5–1.2 V.

With this knowledge, it is possible to set up an automated measurement system that sweeps θ and V_{dc_B} and gathers simultaneously i_{dc_A}, i_{dc_B}, V_{dc_A}, V_{dc_B}, i_{coil_A}, i_{coil_B}, v_{ds_A}, v_{c2_A} and the amplitude of extracted harmonics information from v_{c2} (amplitude of first harmonic H_1, amplitude of second harmonic H_2, and phase between the two PH_{12}). An alternative version of v_{c2} is concurrently extracted through the subsampling method described in Section III-A.

A characterization boundary is determined as shown in Fig. 8 to ensure safe operation of both transceivers under the different loading conditions. The boundary is obtained by setting a maximum transistor temperature of 65 °C under stable cycle-by-cycle operation. While it is possible to use more stringent sets of rules for setting the boundary, such as looking directly at hard-switching or soft switching conditions or maximum current through the device, temperature, and stability are the minimum requirements to ensure safe operation of the system.

A total of 3327 points are gathered to generate the different models. As expected, the system's efficiency is maximized ($\eta = 72.5\%$) when the real portion of the induced voltage is

Tuning of Transceivers A and B through an in-house algorithm

↓

Transceivers A and B are allocated in the bidirectional test rig setup controlled through MATLAB

↓

θ, V_{dc_B} and k are changed to produce controllable changes in v_M

⤙ - - →

The first time the system is powered on, a safe region of operation is found experimentally by establishing the limits on θ and V_{dc_B} for a particular k such that the transistor temperature does not surpass 65° under stable cycle-by-cycle operation

↓

Electrical system parameters are measured at each iteration: i_{dc_A}, i_{dc_B}, V_{dc_A}, V_{dc_B}, i_{coil_A}, i_{coil_B}, v_{ds_A}, v_{c2_A} and the amplitude of the extracted harmonics information from v_{c2}

↓

Electrical system parameters measured on the primary side are assessed using cross-correlation with the real and imaginary parts of v_M

↓

The model is generated through the MATLAB Regression Learner toolbox using the selected set of primary-side variables

- - - →

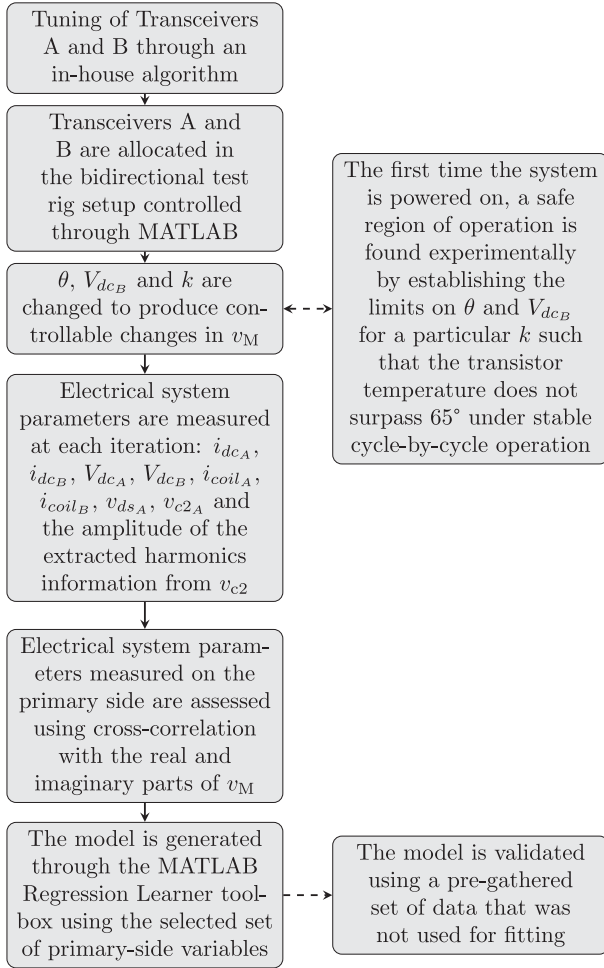The model is validated using a pre-gathered set of data that was not used for fitting

Fig. 9. Design method and procedures flowchart.

maximized and the imaginary portion of the induced voltage is minimized. While it is expected that this would occur for $\theta = -90°$, experiments show that this condition holds for $\theta = -85°$, $V_{dc_A} = V_{dc_B} = 80$ V. The 5° deviation from the expected value of θ can be explained as a slight tuning mismatch between the two sides.

The complete design method and procedures are summarized in Fig. 9.

V. STATISTICAL ANALYSIS OF CANDIDATE WAVEFORMS FOR OPTIMAL MODEL PREDICTION

In data science, a feature is defined as an individual property of a system which can be used to define the system's characteristics. In this article, the features are individual samples of a waveform in the time domain, or steady values representing information such as input current or amplitudes and phases of the harmonics of the switching waveforms. The approach described in our previous work [21] relies on extracting four periods of v_{ds} from an oscilloscope and using every sampled point of the waveform as a feature to estimate both real and imaginary components of v_M. Here, we attempt to build a reduced model by first analyzing the waveforms of the Class EF transceiver operating

over the entire load spectrum to determine which features of the waveform carry the most information about v_M. We analyzed both v_{ds} and v_{c2} in the time-domain and in the frequency-domain and weighted the loading information content using the cross-correlation approach suggested in [40]. We aim to find features that strongly correlate with the real and imaginary parts of v_M, while having low cross-correlation (i.e., redundancy) with each other.

Correlation between two vectors ($\bar{X}$ and $\bar{Y}$) is defined as

$$G \triangleq E[\bar{X}\bar{Y}^T] \tag{1}$$

with $E[\bar{X}\bar{Y}^T]$ being the expectation of the vector product $\bar{X}\bar{Y}^T$. For the analysis conducted in this article, we will use the magnitude of G, since the negative correlation will only indicate that one variable is decreasing as the other variable increases.

These features are then grouped to form datasets that will later be used to generate a regression model used to describe variations of v_M under different loading conditions.

A. Time-Domain Analysis

In this section, the contribution of these individual features of v_{ds} and v_{c2} is first analyzed using the correlation approach described above. Similarly to [21], this section analyzes a dataset extracted with an oscilloscope. Since the goal of this section is oriented around the analysis of the information content of the waveforms, the subsampling is temporarily omitted to ensure that the analysis is performed on the highest quality data. With this analysis, it is possible to assess the presence of regions with high information density, providing a deeper understanding on the effect of v_M on specific time windows within a cycle of the switching waveforms.

A key difference in the comparison of the data from the time domain and the frequency domain is continuity of adjacent features: This occurs in the time-domain since neighboring points in a sampled waveform show a degree of correlation. While all the points on the main diagonal from Fig. 10(a) and 11(a) show a cross-correlation of unity (i.e., the points are self-correlated as expected), it is possible to also notice additional points in proximity of the main diagonal which are strongly correlated in both v_{ds} and v_{c2}. The regions in which the main diagonal gets thinner indicate a portion of the waveform where neighboring features are less correlated. This indicates a nonlinear relationship between features in a specific portion of the waveform. If this occurs for features that are meaningful for the output of the model (i.e., high correlation with the real and imaginary components of v_M), sampling jitter of the extracted switching waveform will have a noticeable effect on the outcome of the estimation of v_M. This problem does not occur in the frequency domain datasets: The harmonic components are independent of sampling jitter since they are individually extracted as steady values.

It is possible to observe that over the same number of features (i.e., same sampling rate in the same time window), v_{ds} presents a region (when the transistor is ON) in which features do not correlate to either EMF_{Im} or EMF_{Re}, meaning that overall the
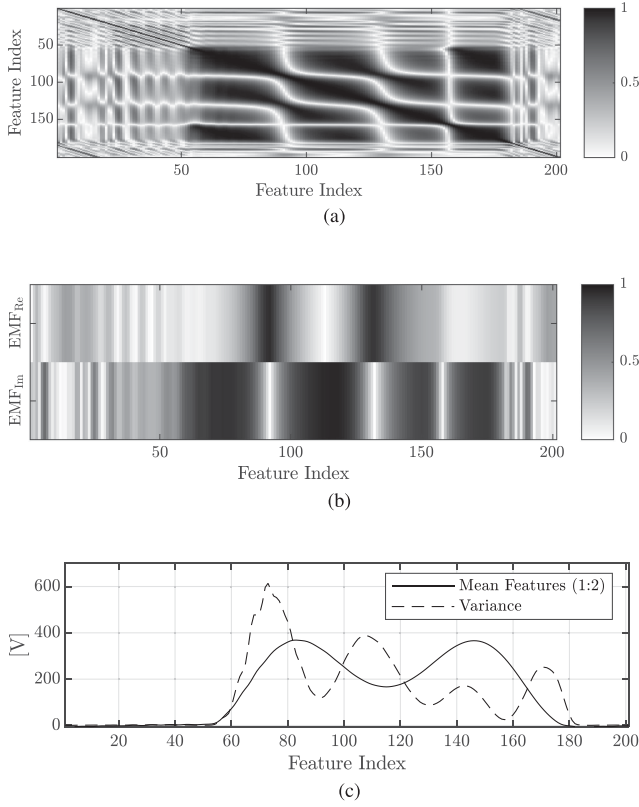
Fig. 10.   Cross-correlation of the time points (feature indexes) and mean of the features in v_{ds}. (a) Absolute value of cross-correlation ($|\mathrm{G}|$) of v_{ds} dataset features to dataset features. (b) Absolute value of correlation ($|\mathrm{G}|$) of v_{ds} dataset features to $\boldsymbol{v}_{\mathbf{M}}$ components. (c) Mean of the features of v_{ds} in the time domain and their associated variance.

Fig. 11.   Cross-correlation of the time points (feature indexes) and mean of the features in v_{c2}. (a) Absolute value of cross-correlation ($|\mathrm{G}|$) of v_{c2} dataset features to dataset features. (b) Absolute value of correlation ($|\mathrm{G}|$) of v_{c2} dataset features to $\boldsymbol{v}_{\mathbf{M}}$ components. (c) Mean of the features of v_{c2} in the time domain and their associated variance.

gathered data contains portions that are not relevant for model generation. Such features will be suppressed in the model.

Another noticeable difference between v_{ds} and v_{c2} is features variance. At turn-OFF v_{ds} will have a high maximum $|\mathrm{d}v/\mathrm{d}t|$, leading to significant changes in a relatively short time window. This translates into a big variation of neighboring data samples, especially when waveform triggering occurs at slightly different times. v_{c2} variations are typically much smaller due to the presence of the LC combination slowing down its rate of change, making features variance more uniform compared to v_{ds}. This can overall reduce the noise introduced by jitter into the dataset, leading to a more robust model.

While it is possible to trigger measurements focused on regions with a high density of information for the estimation of $\boldsymbol{v}_{\mathbf{M}}$ [dark areas in the middle plots of Figs. 10(b) and 11(b)], the maximum correlation of $\boldsymbol{v}_{\mathbf{M}}$ with an individual time-domain feature in v_{ds} and v_{c2} does not surpass 0.95, suggesting the need of additional features to achieve a performance which is comparable to that of other models presented in this article. In Section VI, Table III, it is shown that an attempt of induced voltage estimation using six samples of v_{ds} in the time-domain achieves an acceptable performance, but the overall quality of the model is lower compared to most of the other models presented.

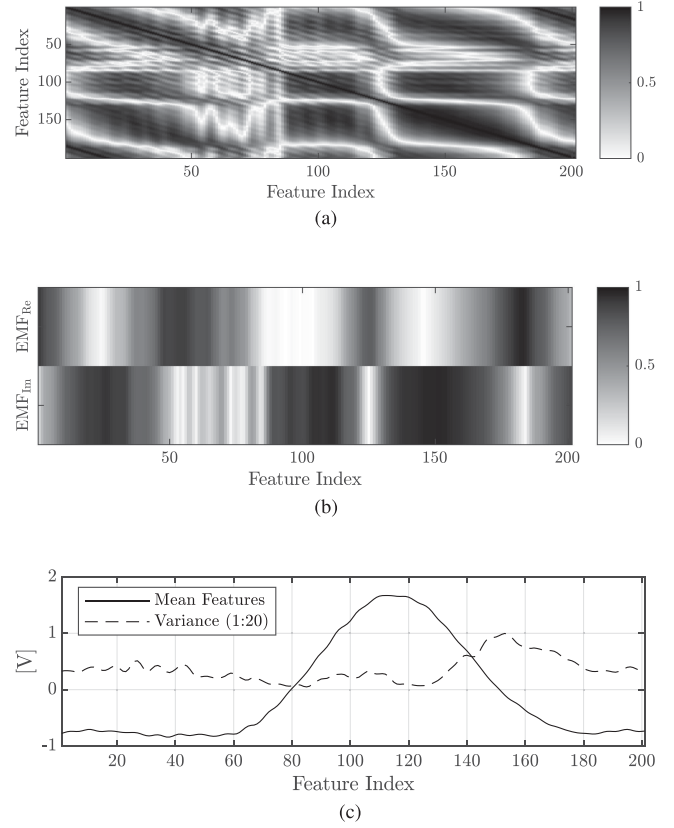It is possible to conclude that the datasets based in the time-domain present significant disadvantages that are difficult to overcome: The dataset can be relatively large for a single cycle of the waveform, measurements can be affected by sampling jitter, and there is a large degree of redundancy carried by multiple features.

B. Frequency-Domain Analysis

The frequency-domain approach poses a valuable alternative to the time-domain approach: The sampling jitter problem is eliminated, individual features that are strongly correlated with the output can be selected more easily, and the induced voltage estimation time decreases since it is not necessary to iterate through several cycles of the waveform to perform subsampling. In this frequency-domain approach, the total speed depends on the time constant of the low-pass filters used for envelope detection and phase retrieval. The data extracted from the harmonics of v_{c2} are analyzed using the same cross-correlation criterion.

As shown in Fig. 12, the feature in v_{c2} with the strongest correlation with the real part of $\boldsymbol{v}_{\mathbf{M}}$ ($\mathrm{EMF}_{\mathrm{Re}}$) is the phase between first and second harmonic (PH_{12}). The amplitudes of first and second harmonic (H_1 and H_2 respectively) are good variables for the estimation imaginary part of $\boldsymbol{v}_{\mathbf{M}}$ ($\mathrm{EMF}_{\mathrm{Im}}$); however, the high cross-correlation between them suggests that the presence of both features in a model will carry redundancies (i.e., the information content of the two features is too similar).
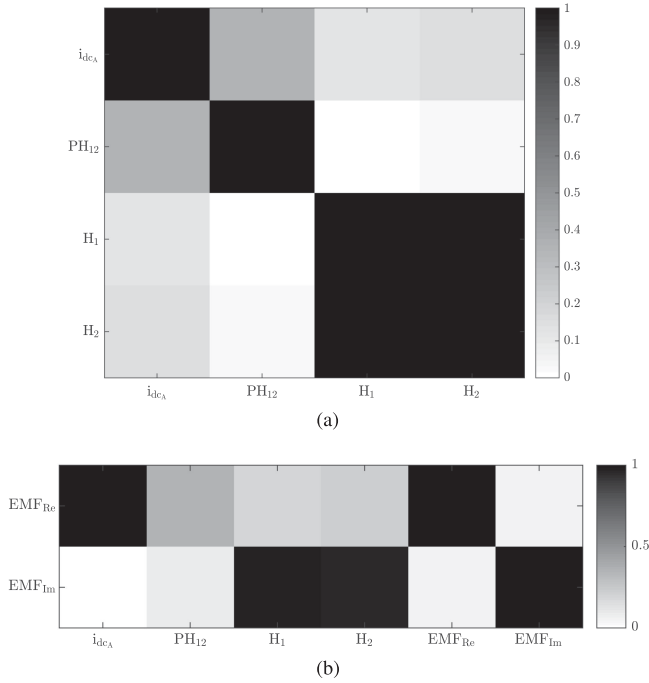
(a)

(b)

Fig. 12. Absolute value of cross-correlation ($|G|$) of dc dataset features (i_{dc_A} transceiver's input current, H_1 amplitude of first harmonic in v_{c2}, H_2 amplitude of second harmonic in v_{c2}, PH_{12} phase between first and second harmonic in v_{c2}). (a) Cross-correlation between dc dataset features. (b) Correlation of measured dc dataset features with v_M components.
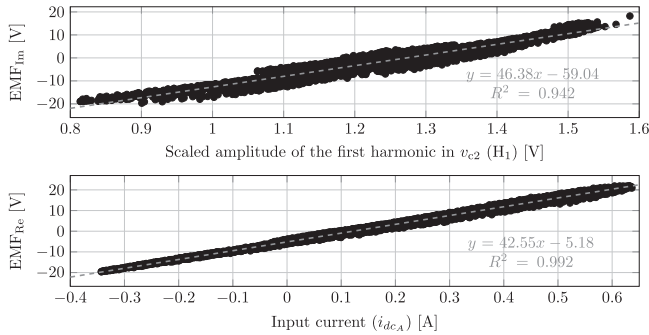

Fig. 13. v_M components plotted against i_{dc_A} and H_1.

In the same cross-correlation matrix, we also analyze the effect of a feature that is not extracted from v_{c2}: The input current of Transceiver A (i_{dc_A}). This feature shows the strongest correlation with EMF_{Re}, making it another suitable variable to perform v_M estimations through the model. This is ultimately expected, since the input current is directly proportional to the real power delivered to a load.

When choosing the best set of features, it is expected that the pair i_{dc_A}-H_1 will outperform the other combinations. This is intuitive when looking at the linear dependency of these features with EMF_{Re} and EMF_{Im}, shown in Fig. 13. While it is also possible to use H_2 rather than H_1, or even a combination of the two, the high correlation between them and the stronger correlation between EMF_{Im} and H_1 indicate that H_1 is overall a better variable to estimate EMF_{Im}. H_1 is also easier to extract, since the bandpass filter is easier to tune and has a much smaller

attenuation, preventing the need of further amplification before envelope detection.

The same analysis and selection process based on cross-correlation can be applied to any of the other switching waveforms (i.e., v_{ds}): In the experimental section of this article, we have also reported an example of induced voltage estimation using the harmonics of v_{ds} rather than v_{c2}. A similar approach based on v_{ds} can be used in the class E topology due to the absence of the v_{c2} waveform (the EF branch is not present). Analysis of the cross-correlation matrix can also be used for other power architectures, but it should not be assumed that the most suitable features will always be i_{dc_A}-H_1. Circuit topology and tuning will affect the cross-correlation matrix, potentially leading to a high amount of information content being carried by the phase component or even the magnitude of higher order harmonics.

In the data presented here, it should be noted that the cross-correlation between the real and imaginary components of the induced voltage on the primary is close to zero. This occurs because the induced voltage was generated through a controlled bidirectional system, which allowed the angle and the magnitude of v_M to be changed independently from each other. When foreign objects are coupled to the transceiver, this is not the case: An object with fixed size and electromagnetic properties will induce a voltage with an angle which is almost constant, but with a magnitude that varies depending on coupling. Obtaining a dataset only through the use of foreign objects will introduce some degree of correlation between the real and imaginary components of v_M.

VI. GENERATION AND EVALUATION OF MODELS

Eight regression models were generated using different combinations of the extracted datasets, both for the time-domain and the frequency-domain to obtain a performance comparison. The reported regression models use a Gaussian process as it was observed that this fitting process tended to outperform support vector machines, linear regressions, and regression trees with all the datasets. Model performance was assessed by gathering 600 additional random points at three different couplings: 1.6% ($k1$), 3.2% ($k2$), and 4% ($k3$). $k3$ is considered an outlier test-set, as the model edge is approached in multiple instances.

A. Calibration

System training and testing does not guarantee top performance under all conditions. Placing the coil in an environment that is different from the training setup may alter the results. This is because changes in the placement of any metallic objects or even elements in the circuit boards (i.e., heath sinks and connectors) may induce a voltage on the coil during system operation. For this reason, a calibration process is required when the system position is altered. An additional set of data is gathered upon operation in the new environment. The reference v_M (calculated knowing the coupling between coils, their inductance, and their currents) is compared with the predictions from the model. For a large enough set of data, the average error of the model should be centered around zero. When this is not the case, it means
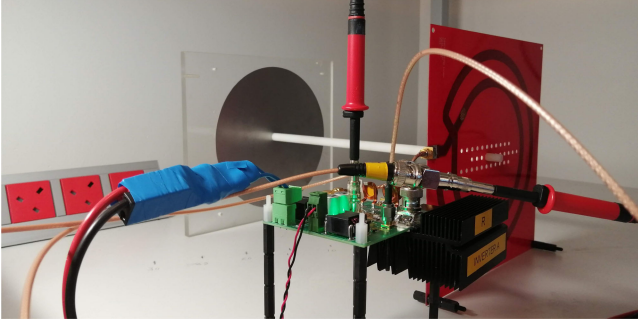
Fig. 14.   Experimental setup for impedance estimation using metallic disks.

TABLE III
MODEL ERRORS. $\mathcal{N}$ WITHIN INNER FIT REGION, $\mathcal{O}$ CLOSE TO OUTLIERS

Model	$\overline{|\boldsymbol{Err}|}$ $\mathcal{N}$	$\overline{|\boldsymbol{Err}|}$ $\mathcal{O}$	max($|\boldsymbol{Err}|$) $\mathcal{N}$	max($|\boldsymbol{Err}|$) $\mathcal{O}$
Scope v_{c2}	0.87	1.30	2.90	4.10
Scope v_{ds} [21]	0.80	1.63	3.00	5.60
Scope v_{ds} 6 points	0.92	1.38	4.09	4.60
Scope H$_{1,2}$−PH$_{12}$ v_{c2}	1.00	2.80	6.00	8.30
Scope H$_{1,2}$−PH$_{12}$ v_{ds}	0.81	1.10	3.00	2.94
Subsampling v_{c2}	0.69	1.84	5.40	7.70
Extracted H$_{1,2}$−PH$_{12}$ v_{c2}	0.81	1.47	3.60	4.30
Extracted i_{dc_A}−H$_1 v_{c2}$	**0.54**	**0.77**	**1.80**	**2.50**

TABLE II
IMPEDANCE ESTIMATION OF METAL DISKS

Disk diameter [cm]	Material	Distance from TX coil [cm]	$X_{\mathcal{M}}$ [Ω]	$X_{\mathcal{P}}$ [Ω]	$|Err|$ [Ω]	σ [Ω]
5	Steel	5.1	0.298	0.315	0.017	0.020
5	Aluminium	5.1	0.247	0.326	0.079	0.020
10	Steel	5.1	1.789	1.700	0.089	0.025
10	Aluminium	5.1	1.789	1.744	0.045	0.017
5	Steel	10.2	0.128	0.005	0.122	0.004
5	Aluminium	10.2	0.119	0.014	0.105	0.022
10	Steel	10.2	0.315	0.315	0.001	0.010
10	Aluminium	10.2	0.324	0.307	0.017	0.005
20	Steel	10.2	1.363	1.424	0.061	0.001
20	Aluminium	10.2	1.389	1.424	0.035	0.008
10	Steel	15.2	0.060	0.068	0.008	0.012
10	Aluminium	15.2	0.060	0.070	0.011	0.003
20	Steel	15.2	0.298	0.381	0.083	0.005
20	Aluminium	15.2	0.307	0.402	0.095	0.004

$\mathcal{M}$ indicates measured impedance from impedance analyzer and $\mathcal{P}$ indicates estimated impedance from the regression model.

a systematic offset is introduced by surrounding objects. This offset can be subtracted from the prediction to adapt the model for the new environment.

A further calibration procedure can be performed when a very precise measurement of v_{M} is required. It is possible to measure the reflected impedance of a given object (in this case, metal disks as a reference fixture) at a fixed coupling from the receiver coil with an impedance analyzer. The reflected impedance (Z_{M}) is obtained by dividing v_{M} by the coil current. These values are then cross-checked with the prediction of the same object from the model. These measurements are performed for three different coupling factors using aluminum and steel disks of different diameters, as shown in Fig. 14 and Table II. Comparing the measured impedance with the predicted impedance allows fitting of a function that approximates the error with respect to the measured impedance. In the performed experiments, the function appeared to be linear. The predicted value can then be scaled according to the function. This allows corrections to be made to variables that are hard-coded in the model (e.g., coil inductance and coupling).

Table II presents the impedance estimation results for the calibrated i_{dc_A}-H$_1$ model. The maximum errors (122 mΩ in the worst case) are obtained for tests where the reflected impedance

on the primary is extremely low, making it difficult to distinguish between an unloaded scenario and the presence of small metallic disks (5-cm diameter) at a distance of 10.2 cm from the primary coil. The standard deviation of the readings does not surpass 25 mΩ. For metallic disks larger than 10 cm in diameter, the reflected impedance is estimated with errors lower than 100 mΩ for separations ranging from 5.1 to 15.2 cm.

B. Comparison of Models

The following results are obtained after calibrating the system using the offset-correction method. Table III confirms that models that are based on time-domain datasets have similar performances. The model based on v_{c2} has better average performance than v_{ds} in the inner fit region, while its average performance around outliers is slightly worse.

Interestingly, the model obtained through subsampling of v_{c2} has a higher average performance than the one obtained from direct scope measurements in the inner fit region, while performing worse around outliers and in terms of maximum error. Averaging of multiple individual samples with the subsampling method leads to a more precise measurement of the waveform since high-frequency noise is attenuated; however, the equivalent time resolution obtained with this method, set by the delay line's minimum time-step, is lower than the one of the oscilloscopes (2 GHz for subsampling and 2.5 GHz for the oscilloscopes). Moreover, the time-step of the delay line used for this method is not perfectly linear, causing distortion to the reconstructed waveform along the x-axis. This leads to the different performance of the two models depending on the operating region.

The combination of the three dc features obtained from the harmonics (H$_1$, H$_2$, PH$_{12}$) closely matches the performance of the time domain models, but considering that overall the number of features is much smaller, this method is much more practical in terms of implementation.

The best model is obtained from the i_{dc_A}-H$_1$ pair. Its error is close to half the error of all the other models, even around outliers. While other combinations of i_{dc_A} with H$_1$, H$_2$, and PH$_{12}$ were tested, i_{dc_A}-H$_1$ slightly outperformed the other models, confirming the hypothesis formulated in Section V-B.

The average response times of the models range from 120 ms (for models relying on 2 input variables) to 150 ms (for models relying on more than 200 input variables).
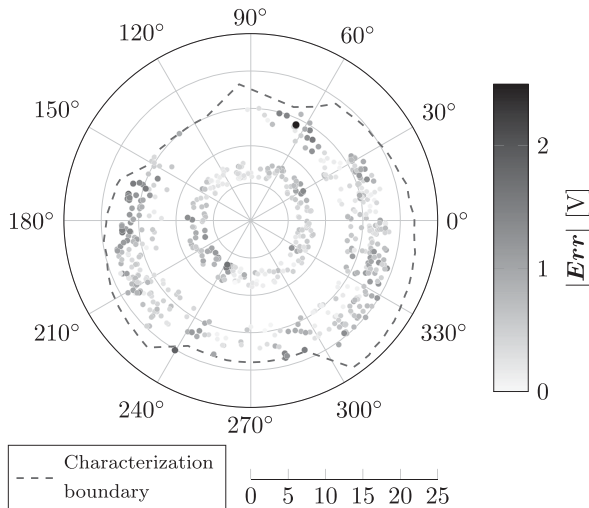
Fig. 15. Phasor chart representing the magnitude of the prediction error in the i_{dc_A}-H$_1$ model.

TABLE IV
BOM FOR i_{DC_A}-H$_1$ BOARD. THE PHASE RETRIEVAL COMPONENTS ARE
IGNORED SINCE THIS METHOD DOES NOT USE INFORMATION ON THE PHASE

Component	MPN	Quantity	Total Price (USD)
Operational amplifier	AD8091ARZ	4	9.08
Crystal	449-LFXTAL014948BULK	2	1.40
Diode	MMDL301T1G	2	0.58
Resistor	Generic	10	0.30
Capacitor	Generic	10	0.30
Microprocessor	EK-TM4C123GXL	1	15.59
Total			27.25

As reported in Table III and Fig. 15, the error of the model depends on the operating region: When the system operation is close to the model's boundary (i.e., high loading conditions), the error increases. This mainly occurs because the system characterization has been performed in a region in which the coil driver operation is deemed safe and stable. Approaching the boundary pushes the model into a region that becomes closer to an interpolation rather than a fit, which leads to higher errors, especially in models in which linearity of input-to-output variables is not maintained. Moreover, this can lead to heating of the device, altering the performance of the coil driver. This error dictates the sensitivity of the proposed induced voltage estimation technique. To perform a reliable measurement, the change in induced voltage needs to be larger than the average error. From Table III, the sensitivity of the model based on the i_{dc_A}-H$_1$ pair ranges from 0.54 to 0.77 V, depending on the region of operation. This is further validated from the FOD data in Fig. 16, in which 100% detection accuracy is only achieved when the change in the imaginary part of v_{M} is larger than 0.5 V.

The results in the following sections are obtained using the model based on the i_{dc_A}-H$_1$ pair since it is simpler than the other models, easier to integrate and achieves the best performance.
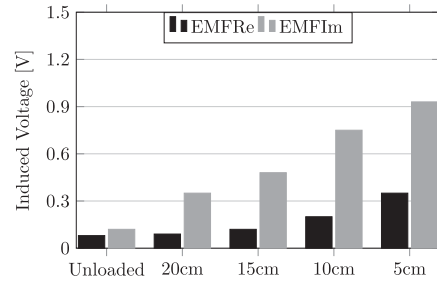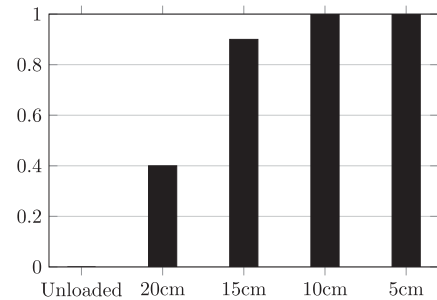
Fig. 16. Model predictions for detection of 1 kg of saline solution at different distances. (a) Induced voltage prediction (ten samples average). (b) Detection accuracy with a single measurement (ten samples average).
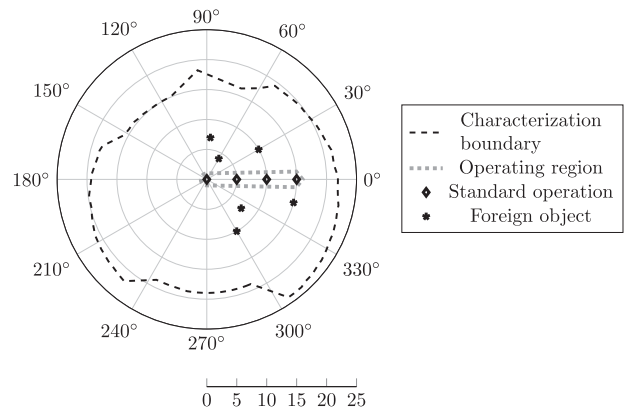

Fig. 17. Phasor chart representing the proposed FOD strategy based on definition of an operating region.

VII. PRACTICAL APPLICATIONS OF THE PROPOSED v_{M} MEASUREMENT TECHNIQUES

The v_{M} predictions obtained through the proposed i_{dc_A}-H$_1$ model can be used for multiple purposes.

A. Foreign Object Detection

FOD is an interesting application of this concept, since deviations from the expected v_{M} are either caused by faults or by foreign objects. As shown in Fig. 17, it is possible to set an inverter operating region within the characterization boundary. This region is obtained as all the expected operating conditions for a set of given loads. The expected v_{M} is real and positive for a transceiver sending power. When a measured point falls

TABLE V
MINIMUM SIZE OF DETECTABLE FOREIGN OBJECTS FOR A GIVEN DISTANCE
FROM TRANSCEIVER'S COIL

Distance from Transceiver's Coil Normalised to Coil Diameter	Smallest Object Detected
1	Circular Aluminium Disk, Diameter = 15 cm
0.5	Circular Aluminium Disk, Diameter = 7.5 cm
0.25	2 GBP Coin Covered in Aluminium Foil, Diameter ≃ 3 cm
≃ 0	Copper Washer, Diameter = 1 cm

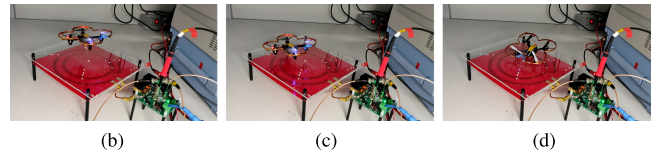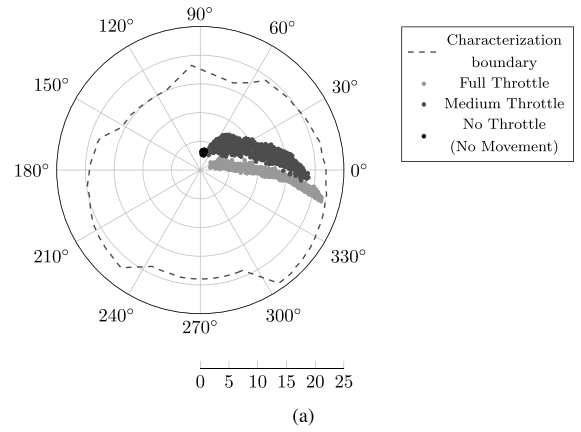(a)

(b)   (c)   (d)

Fig. 18. Induced voltage estimations to profile dynamic loads using the batteryless drone of [6]. (a) Phasor chart representing the induced voltage estimations for the different possible loads of the system under different operating conditions. (b) Full throttle. (c) Medium throttle. (d) No throttle.

outside of this region, the inverter is not operating as expected: If EMF_{Re} is too large, it means the inverter is probably overloaded, while if EMF_{Im} is higher or lower than the model's maximum error (2.5 V), it means a foreign object is detected. A foreign object that reflects a positive EMF_{Im} indicates that the element coupled to the coil has an equivalent capacitive impedance, while a foreign object that reflects a negative EMF_{Im} has an inductive one.

In the experimental data reported in Fig. 16, it is shown how the FOD setup performs for a plastic container filled with 1 kg of saline solution at a 0.4% concentration to emulate the electromagnetic profile of muscle. This aims to replicate the presence of human body tissues in proximity of the coil.

It is possible to notice that a variation in induced voltage is detected even at a distance of 20 cm; however, the standard deviation of the model prediction does not make it possible to capture this variation reliably within one measurement, leading to a less sensitive model. Subsequent measurements can be taken to improve the model's accuracy, increasing the instrument sensitivity at the cost of slower response times: Taking the average of three measurement would lead to a 99.9% detection accuracy even for a distance of 15 cm, but the response time would increase from 120 to 360 ms.

The size of the smallest detectable foreign objects using this system is a function which depends on the material of the foreign object and its distance from the transceiver's coil. Table V reports examples of the minimum detection size of metallic objects as a function of distance from the unloaded transceiver. The data reported in Table V are based on a single-measurement assessment.

B. Synchronization of Active Rectifiers and Bidirectional Systems

Knowing the angle of v_M allows for correction of the phase between transceivers. Assuming a matched switching frequency of the two transceivers, phase correction for operation at unity power factor can be performed in a single step.

While it is possible to perform subsequent corrections to improve accuracy and decrease the imaginary component of v_M, the model's standard deviation and offset on EMF_{Im} predictions will dictate the minimum achievable angle error.

This approach can be advantageous in synchronization techniques that require a search algorithm for optimal phase identification [41], [42]. Most of these techniques rely on sweeping the phase value and estimate the optimal relative phase between

transceivers. For high-coupling conditions, this phase sweep could be unfeasible due to the detuning of either of the two transceivers, leading to potential heating and circuitry damage. Using the method proposed in this article would instead make it possible to achieve a fast convergence time without detuning the system.

This article has a multimedia object which includes examples of synchronization of an active rectifier at a coupling of 1.6%. In the conducted experiments, the magnitude of the angle error did not exceed $10°$.

C. Load Profiling of Highly Dynamic Systems

The presented technique can also be used to analyze the behavior of systems in which fast but bounded load changes occur. Since the response time is in the hundreds-of-milliseconds, it is difficult to capture step changes in load. However, for systems in which such changes occur with a particular pattern (i.e., the batteryless drone of [6]), it is possible to perform a series of measurements to obtain a complete load profile of the system. This can be used to quantify the probability distribution of loads, enabling further applications of the tuning techniques based of the expectation of k as discussed in [4]. Another advantage of load profiling is the possibility of obtaining an experimental region of operation with the purpose of fault detection or FOD (similarly to the concept highlighted in Fig. 17).

In Fig. 18, we show experimental results using the same batteryless drone presented in [6] as a load. The load profile of the implemented receiver using a hybrid Class E rectifier validates the results presented in [26], with an expected peak in reflected reactance for low load conditions and a load which is almost purely resistive at full throttle. From Fig. 18, it is possible

to identify that the different levels of throttle in the receive unit affect the probability distribution of the coupling factor, leading to the core differences in shape between the three presented operating regions. The second multimedia object of this article includes an example of real-time load-profiling for the presented system powering the drone.

VIII. CONCLUSION

The induced voltage in IPT systems provides valuable information about the interaction between the system's primary side and the environment, including tuned receivers and foreign objects. Unfortunately, this induced voltage is not directly measurable when the system is in operation.

In this article, we have presented two techniques for the estimation of the induced voltage in the coil of a Class EF-based transceiver, which uses cost-effective components allowing the techniques to be deployed in real systems. The first, based in the time domain, reconstructs the switching waveform through subsampling rather than using a high-performance oscilloscope. The second technique, based in the frequency domain, analyzes the information content in the amplitude and phase of the first two harmonics of the waveform. We found that with a combination of i_{dc} and H_1, we were able to produce the most accurate estimate of v_M. This model is also the fastest and the one with the highest data-density. The individual candidate variables were assessed following a statistical approach to quantify correlation with the real and imaginary parts of the induced voltage.

We have shown that, in a bidirectional system, v_M can be estimated with a maximum error of 2.5 V (6%) and an average error of 0.62 V (1.6%) using exclusively two measurable variables extracted as dc voltages. The measurement process can be fast (120 ms), making it suitable for applications where a quick response time is required.

Reflected impedance estimations can be performed with a maximum error of 122 mΩ. Phase synchronization of active transceivers can be achieved quickly and accurately with angle errors lower than 10° in a single adjustment step. Foreign object detection can be reliably performed at a distance of one coil diameter with both metallic objects and salt water.

REFERENCES

[1] J. Choi, D. Tsukiyama, Y. Tsuruda, and J. Rivas, "13.56 MHz 1.3 kW resonant converter with GaN FET for wireless power transfer," in *Proc. IEEE Wireless Power Trans. Conf.*, 2015, pp. 1–4.

[2] M. Liu, S. Liu, and C. Ma, "A high-efficiency/output power and low-noise megahertz wireless power transfer system over a wide range of mutual inductance," *IEEE Trans. Microw. Theory Techn.*, vol. 65, no. 11, pp. 4317–4325, Nov. 2017.

[3] G. Zulauf and J. M. Rivas Davila, "Single-turn air-core coils for high-frequency inductive wireless power transfer," *IEEE Trans. Power Electron.*, vol. 35, no. 3, pp. 2917–2932, Mar. 2020.

[4] J. M. Arteaga, S. Aldhaher, G. Kkelis, D. C. Yates, and P. D. Mitcheson, "Multi-MHz IPT systems for variable coupling," *IEEE Trans. Power Electron.*, vol. 33, no. 9, pp. 7744–7758, Sep. 2018.

[5] N. Pucci, C. H. Kwan, D. C. Yates, and P. D. Mitcheson, "Multi-megahertz IPT systems for biomedical devices applications," in *Proc. Int. Conf. Micro Nanotechnol. Power Gener. Energy Convers. Appl.*, 2019, pp. 1–7.

[6] J. M. Arteaga, S. Aldhaher, G. Kkelis, C. Kwan, D. C. Yates, and P. D. Mitcheson, "Dynamic capabilities of multi-MHz inductive power transfer systems demonstrated with batteryless drones," *IEEE Trans. Power Electron.*, vol. 34, no. 6, pp. 5093–5104, Jun. 2019.

[7] C. H. Kwan, J. M. Arteaga, D. C. Yates, and P. D. Mitcheson, "Design and construction of a 100 W wireless charger for an E-scooter at 6.78 MHz" in Proc. *IEEE PELS Workshop Emerg. Technol. Wireless Power Trans.*, 2019, pp. 186–190.

[8] L. Lan, C. H. Kwan, J. M. Arteaga, D. C. Yates, and P. D. Mitcheson, "A 100 W 6.78 MHz inductive power transfer system for drones," in *Proc. Eur. Conf. Antennas Propag.*, 2020, pp. 1–4.

[9] A. Kurs, A. Karalis, R. Moffatt, J. D. Joannopoulos, P. Fisher, and M. Soljačić, "Wireless power transfer via strongly coupled magnetic resonances," *Science*, vol. 317, no. 5834, pp. 83–86, 2007.

[10] M. Pinuela, D. C. Yates, S. Lucyszyn, and P. D. Mitcheson, "Maximizing DC-to-load efficiency for inductive power transfer," *IEEE Trans. Power Electron.*, vol. 28, no. 5, pp. 2437–2447, May 2013.

[11] S. Aldhaher, D. C. Yates, and P. D. Mitcheson, "Load-independent class E/EF inverters and rectifiers for MHz-switching applications," *IEEE Trans. Power Electron.*, vol. 33, no. 10, pp. 8270–8287, Oct. 2018.

[12] W. D. Braun and D. J. Perreault, "A high-frequency inverter for variable-load operation," *IEEE Trans. Emerg. Sel. Topics Power Electron.*, vol. 7, no. 2, pp. 706–721, Jun. 2019.

[13] A. Kumar, S. Sinha, and K. K. Afridi, "A high-frequency inverter architecture for providing variable compensation in wireless power transfer systems," in *Proc. IEEE Appl. Power Electron. Conf. Expo.*, 2018, pp. 3154–3159.

[14] Y. Han, O. Leitermann, D. A. Jackson, J. M. Rivas, and D. J. Perreault, "Resistance compression networks for radio-frequency power conversion," *IEEE Trans. Power Electron.*, vol. 22, no. 1, pp. 41–53, Jun. 2007.

[15] G. Kkelis, D. C. Yates, and P. D. Mitcheson, "Class-E half-wave zero dv/dt rectifiers for inductive power transfer," *IEEE Trans. Power Electron.*, vol. 32, no. 11, pp. 8322–8337, Nov. 2017.

[16] K. Li, S. Tan, and R. S. Y. Hui, "Single-switch-regulated resonant WPT receiver," *IEEE Trans. Power Electron.*, vol. 34, no. 11, pp. 10386–10391, Nov. 2019.

[17] G. A. Covic and J. T. Boys, "Modern trends in inductive power transfer for transportation applications," *IEEE Trans. Emerg. Sel. Topics Power Electron.*, vol. 1, no. 1, pp. 28–41, Mar. 2013.

[18] S. Li and C. C. Mi, "Wireless power transfer for electric vehicle applications," *IEEE J. Emerg. Sel. Topics Power Electron.*, vol. 3, no. 1, pp. 4–17, Mar. 2015.

[19] A. Zaheer, M. Neath, H. Z. Z. Beh, and G. A. Covic, "A dynamic EV charging system for slow moving traffic applications," *IEEE Trans. Transport. Electrific.*, vol. 3, no. 2, pp. 354–369, Jun. 2017.

[20] D. Patil, M. K. McDonough, J. M. Miller, B. Fahimi, and P. T. Balsara, "Wireless power transfer for vehicular applications: Overview and challenges," *IEEE Trans. Transport. Electrific.*, vol. 4, no. 1, pp. 3–37, Mar. 2018.

[21] J. M. Arteaga, N. Pucci, L. Lan, and P. D. Mitcheson, "Load characterization in high-frequency IPT systems using class EF switching waveforms," *IEEE Trans. Power Electron.*, vol. 36, no. 10, pp. 11036–11044, Oct. 2021.

[22] Y. Zhang, Z. Yan, J. Zhu, S. Li, and C. Mi, "A review of foreign object detection (FOD) for inductive power transfer systems," *eTransportation*, vol. 1, 2019, Art. no. 100002.

[23] S. Y. R. Hui, W. Zhong, and C. K. Lee, "A critical review of recent progress in mid-range wireless power transfer," *IEEE Trans. Power Electron.*, vol. 29, no. 9, pp. 4500–4511, Sep. 2014.

[24] J. M. Arteaga, L. Lan, S. Aldhaher, G. Kkelis, D. C. Yates, and P. D. Mitcheson, "A multi-MHz IPT-link developed for load characterisation at highly variable coupling factor," in *Proc. IEEE Wireless Power Trans. Conf.*, 2018, pp. 1–4.

[25] L. Lan, J. M. Arteaga, D. C. Yates, and P. D. Mitcheson, "A reflected impedance estimation technique for inductive power transfer," in *Proc. IEEE PELS Workshop Emerg. Technol.*, 2019, pp. 1–4.

[26] J. M. Arteaga, L. Lan, C. H. Kwan, D. C. Yates, and P. D. Mitcheson, "Characterisation of high frequency inductive power transfer receivers using pattern recognition on the transmit side waveforms," in *Proc. IEEE Appl. Power Electron. Conf. Expo.*, 2020, pp. 825–831.

[27] Z. Kaczmarczyk, "High-efficiency class e, EF_2, and E/F_3 inverters," *IEEE Trans. Ind. Electron*, vol. 53, no. 5, pp. 1584–1593, Oct. 2006.

[28] S. Aldhaher, P. D. Mitcheson, and D. C. Yates, "Load-independent class EF inverters for inductive wireless power transfer," in *Proc. IEEE Wireless Power Trans. Conf.*, 2016, pp. 1–4.

[29] M. Neath, U. Madawala, and D. Thrimawithana, "Frequency jitter control of a multiple pick-up bidirectional inductive power transfer system," in *Proc. IEEE Int. Conf. Ind. Technol.*, 2013, pp. 521–526.

[30] R. W. Erickson and D. Maksimovic, *Fundamentals of Power Electronics*. Berlin, Germany: Springer, 2007.

[31] M. Chudobiak, "The use of parasitic nonlinear capacitors in class E amplifiers," *IEEE Trans. Circuits Syst. I, Fundam. Theory Appl.*, vol. 41, no. 12, pp. 941–944, Dec. 1994.

[32] J. Choi, D. Tsukiyama, Y. Tsuruda, and J. M. R. Davila, "High-frequency, high-power resonant inverter with eGaN FET for wireless power transfer," *IEEE Trans. Power Electron*, vol. 33, no. 3, pp. 1890–1896, Mar. 2018.

[33] Bottom-side cooled 650 v. e-mode GaN transistor, GS66504B datasheet, *GaN Syst.*, 2009, rev. 170321.

[34] J. Liu, G. Wang, G. Xu, J. Peng, and H. Jiang, "A parameter identification approach with primary-side measurement for DC–DC wireless-power-transfer converters with different resonant tank topologies," *IEEE Trans. Transport. Electrific.*, vol. 7, no. 3, pp. 1219–1235, Sep. 2021.

[35] S. Ziegler, R. C. Woodward, H. H. Iu, and L. J. Borle, "Current sensing techniques: A review," *IEEE Sensors J.*, vol. 9, no. 4, pp. 354–376, Apr. 2009.

[36] High Voltage Passive Probe Datasheet, PMK, 2020, Rev. 10.2020.

[37] R. G. Kinsman, "A history of crystal filters," in *Proc. IEEE Int. Freq. Cont. Symp.*, 1998, pp. 563–570.

[38] W. Hayward, *Introduction to Radio Frequency Design.* Newington, CT, USA: American Radio Relay League, 1994, pp. 101–108.

[39] N. Pucci, J. M. Arteaga, and P. D. Mitcheson, "Design and development of a test rig for 13.56 MHz IPT systems with synchronous rectification and bidirectional capability," in *Proc. IEEE PELS Workshop Emerg. Technol.*, 2021, pp. 1–5.

[40] M. A. Hall, "Correlation-based feature selection for machine learning," Ph.D. dissertation, Dept. Comput. Sci., Univ. Waikato Hamilton, Hamilton, New Zealand, 1999.

[41] E. Asa, K. Colak, M. Bojarski, and D. Czarkowski, "A novel phase control of semi bridgeless active rectifier for wireless power transfer applications," in *Proc. IEEE Appl. Power Electron. Conf. Expo.*, 2015, pp. 3225–3231.

[42] S. Cochran and D. Costinett, "Frequency synchronization and control for a 6.78 MHz WPT active rectifier," in *Proc. IEEE 19th Workshop Control Model. Power Electron.*, 2018, pp. 1–7.

Nunzio Pucci (Student Member, IEEE) received the M.Eng. degree in electrical and electronic engineering in 2019 from Imperial College London, London, U.K., where he is currently working toward the Ph.D. degree in power electronics and high-frequency wireless power transfer.

His research interests include power electronics, resonant converters, wireless power transfer, custom instrumentation, and machine learning.

Mr. Pucci was a recipient of three conference prizes, including the WoW 2021 IEEE Workshop on Emerging Technologies: Wireless Power Best Paper Prize.

Juan M. Arteaga (Member, IEEE) received the B.Sc. and Licentiate(Hons.) degrees in electrical engineering from the University of Costa Rica, San Pedro, Costa Rica, in 2008 and 2010, respectively, the M.Sc. degree in micro and nanoelectronics from the Autonomous University of Barcelona, Bellaterra, Spain, in 2011, and the Ph.D. degree in electrical and electronic engineering from Imperial College London, London, U.K., in 2020.

His doctoral research focused on the integration of high-frequency inductive power transfer systems into applications.

He is currently a Research Associate with Control and Power Research Group, Department of Electrical and Electronic Engineering, Imperial College London, London, U.K. His research interests include power electronics, high-frequency resonant converters, and wireless power transfer.

Dr. Arteaga was a recipient of the 2019 IEEE Transactions on Power Electronics Second Prize Paper Award and the Eryl Cadwallader Davies Prize for his Ph.D. thesis.

Christopher H. Kwan received the M.Eng. degree in electrical and electronic engineering with management and the Ph.D. degree in electrical engineering from Imperial College London, London, U.K., in 2013 and 2018, respectively.

His doctoral research focused on the design of wireless power transfer systems in the presence of living objects and for implantable medical devices.

He is currently a Senior Electromagnetics Engineer with Bumblebee Power Ltd., London, U.K, and a Visiting Researcher with Control and Power Research Group, Department of Electrical and Electronic Engineering, Imperial College London. His research interests include the design and optimization of inductive power transfer systems for electric vehicles and e-mobility applications.

David C. Yates (Member, IEEE) received the M.Eng. degree in electrical engineering and the Ph.D. degree from Imperial College London, London, U.K., in 2001 and 2007, respectively.

His doctoral thesis was focused on antenna and RF circuit and system design for ultralow-power wireless links.

He is currently the Chief Technology Officer with Bumblebee Power Ltd., London, U.K., and a Visiting Researcher with Wireless Power Lab, Imperial College London. His research interests include HF converters and magnetics for wireless power transfer.

Paul D. Mitcheson (Senior Member, IEEE) received the M.Eng. degree in electrical and electronic engineering and the Ph.D. degree in micropower motion-based energy harvesting for wireless sensor networks from Imperial College London, London, U.K., in 2001 and 2005, respectively.

He is currently a Professor of electrical energy conversion with Control and Power Research Group, Electrical and Electronic Engineering Department, Imperial College London. His research interests include energy harvesting, power electronics, and wireless power transfer to provide power to applications in circumstances where batteries and cables are not suitable. His research has been supported by the European Commission, Engineering and Physical Sciences Research Council, and several companies.

Prof. Mitcheson is a Fellow of the Higher Education Academy and is on the Executive Committee of the U.K. Power Electronics Centre. He was the General Co-Chair of IEEE Wireless Power Week in 2019 in London, U.K.